Implementing Dynamic Boundary Conditions with the Material Point Method

Do, Phuong Chinh; Vardon, Philip J.; González Acosta, José León; Hicks, Michael A.

DOI
10.1007/978-3-031-12851-6_27

Publication date
2023

Document Version
Final published version

Published in
Challenges and Innovations in Geomechanics

Citation (APA)
Do, P. C., Vardon, P. J., González Acosta, J. L., & Hicks, M. A. (2023). Implementing Dynamic Boundary Conditions with the Material Point Method. In M. Barla, A. Insana, A. Di Donna, & D. Sterpi (Eds.), *Challenges and Innovations in Geomechanics: Proceedings of the 16th International Conference of IACMAG* (pp. 221-228). (Lecture Notes in Civil Engineering; Vol. 288 LNCE). Springer. https://doi.org/10.1007/978-3-031-12851-6_27

Implementing Dynamic Boundary Conditions with the Material Point Method

Phuong Chinh Do, Philip J. Vardon(✉), José León González Acosta, and Michael A. Hicks

Geo-Engineering Section, Faculty of Civil Engineering and Geosciences, Delft University of Technology, P.O. Box 5048, 2600 GA Delft, The Netherlands
P.J.Vardon@tudelft.nl

Abstract. The material point method (MPM) is gaining an increasing amount of attention due to its capacity to solve geotechnical problems involving large deformations. Large deformations in geotechnics usually involve the failure process and therefore dynamic analyses are often carried out. However, simulating the (infinite) continuous domain using typical Dirichlet (fixed) boundary conditions induces spurious reflections, causing (1) unrealistic stress increments at the domain boundary and (2) the appearance of multiple unnatural stress waves in the domain. Aiming to eliminate this numerical artifact in MPM, two solutions for absorbing boundary conditions found in FEM are implemented and investigated; these are (1) a viscous boundary condition and (2) a viscoelastic boundary condition. The use of such dynamic boundary conditions in MPM is scarce and no validation of them has yet been presented in the literature. In this paper, these absorbing conditions are implemented alongside recent mapping and integration techniques, improving numerical stability and accuracy.

Keywords: Dynamic boundaries · Double mapping–generalized composite MPM · Implicit MPM · Shallow foundation · Wave propagation

1 Introduction

Since the first release of the material point method (Sulsky et al. 1994), numerous large deformation geotechnical problems have been successfully simulated using this technique, such as CPT penetration (Ceccato et al. 2016), landfill settlement (Zhou et al. 1999) and slope failure (Wang et al. 2016). Despite MPM's advantages, the method's accuracy, particularly in the stress field, is far from the desired level. This problem is commonly manifested as stress oscillations which are mostly caused due to the use of discontinuous finite element (FE) shape function gradients (Bardenhagen et al. 2000; González Acosta et al. 2020). Additionally, another problem often encountered during dynamic simulations is that shear and compression waves are unable to transmit through typical fixed boundaries. This problem, combined with stress oscillations, can significantly result in a poor quality of the MPM solution. In this paper, standard viscous and viscoelastic boundary conditions will be implemented and validated using the MPM

M. Barla et al. (Eds.): IACMAG 2022, LNCE 288, pp. 221–228, 2023.
https://doi.org/10.1007/978-3-031-12851-6_27

framework to eliminate spurious reflections. Section 2 presents the background formulation of the implicit MPM and DM-GC, a technique used to enhance MPM accuracy. Section 3 derives the dynamic boundary formulations, while benchmarks are presented in Sect. 4. Conclusions are drawn in Sect. 5.

2 Background

2.1 Material Point Method

This work employs the implicit MPM formulation used in Wang et al. (2016). The equation of equilibrium, obtained through the principle of virtual work, is written as:

$$\left(\mathbf{K} + \frac{\mathbf{4m}}{\Delta t^2}\right)\Delta\mathbf{u} = \mathbf{F}_{ext} - \mathbf{F}_{int} - \mathbf{F}_{kin} \tag{1}$$

where $\Delta\mathbf{u}$ is the incremental nodal displacement vector, and $\mathbf{K}$ and $\mathbf{m}$ are the global stiffness and mass matrices computed as:

$$\mathbf{K} = \sum_{p=1}^{nmps} \mathbf{B}^{\mathbf{T}}(\mathbf{x}_p)\mathbf{D}\mathbf{B}(\mathbf{x}_p)|J|W_p \tag{2}$$

$$\mathbf{m} = \sum_{p=1}^{\text{nmps}} \rho_p \mathbf{N}^{\mathbf{T}}(\mathbf{x}_p)\mathbf{N}(\mathbf{x}_p)|J|W_p \tag{3}$$

where *nmps* is the number of material points, $\mathbf{B}$ is the strain-displacement matrix, $\mathbf{x}_p$ is the vector of material point coordinates, $\mathbf{D}$ is the material elastic matrix, $|\mathbf{J}|$ is the Jacobian determinant, W_p is the material point integration weight, Δt is the time step, ρ_p is the material point's density and $\mathbf{N}$ is the matrix of shape functions. The vectors of external, internal and kinematic forces (i.e. $\mathbf{F}_{ext}$, $\mathbf{F}_{int}$, $\mathbf{F}_{kin}$, respectively) are computed as:

$$\mathbf{F}_{ext} = \sum_{p=1}^{nmps} \mathbf{N}^{\mathbf{T}}(\mathbf{x}_p)\mathbf{b}|\mathbf{J}|W_p + \sum_{p=1}^{bmps} \mathbf{N}^{\mathbf{T}}(\mathbf{x_p})\mathbf{s}^{\mathbf{s}} \tag{4}$$

$$\mathbf{F}_{int} = \sum_{p=1}^{nmps} \mathbf{B}^{\mathbf{T}}(\mathbf{x}_p)\boldsymbol{\sigma}_p|\mathbf{J}|W_p \tag{5}$$

$$\mathbf{F}_{kin} = \mathbf{m}\left(\frac{\mathbf{4u}}{\Delta t^2} - \frac{\mathbf{4v}}{\Delta t} - \mathbf{a}\right) \tag{6}$$

where $\mathbf{b}$ is the body force (i.e. gravity), $\mathbf{s}^{\mathbf{s}}$ is the traction applied at the boundary, *bmps* is the number of boundary material points where traction is applied, σ_p is the material point stress tensor, and $\mathbf{u}$, $\mathbf{v}$ and $\mathbf{a}$ are the vectors of nodal displacement, velocity and acceleration, respectively.

2.2 DM-GC

To reduce the oscillation of stresses, double mapping (DM), the generalized interpolation material point method (GIMP) and the composite material point method (CMPM) are combined and implemented in one technique, the DM-GC. In this method, the global stiffness matrix is calculated as:

$$\mathbf{K} = \sum_{g=1}^{ngauss} \mathbf{B}^{\mathbf{T}}(\mathbf{x}_{\mathrm{p}}) \left[\sum_{i=1}^{nn} \left(\mathrm{N}_i(\mathbf{x}_g) \sum_{p=1}^{smp} \mathbf{S}_{ip*}(\mathbf{x}_p) \mathbf{D} W_p \right) \mathbf{B}(\mathbf{x}_{\mathrm{p}}) |\mathbf{J}| W^{FE} \right] \tag{7}$$

where *ngauss*, *nn* and *smp* are the number of Gauss integration points in the element, number of nodes of the element and number of material points with a support domain inside the element, respectively, N_i is the nodal shape function, S_{ip*} is the local GIMP shape function and W^{FE} is the finite element weight corresponding to Gauss point g. A detailed elaboration of these equations is found in Gonzalez Acosta et al. (2017) and Gonzalez Acosta et al. (2020).

2.3 Non-reflecting Boundaries

Lymsmer and Kuhlemeyer (1969) proposed the standard viscous boundary which can be expressed in terms of stress condition as:

$$\boldsymbol{\sigma}_{n,s} = -\rho \mathbf{C}_{n,s} \mathbf{v}_{n,s} \tag{8}$$

where $\sigma_{n,s}$ and $\mathbf{v}_{n,s}$ are the vectors of normal and shear stresses and velocities at the boundary, respectively. The wave velocity matrix $\mathbf{C}_{n,s}$ is computed as:

$$\mathbf{C}_{\mathrm{n,s}} = \sqrt{\frac{\mathrm{E}}{\rho(1+\nu)(1-2\nu)}} \begin{bmatrix} (1-\nu) & 0 \\ 0 & (1-2\nu)/2 \end{bmatrix} \tag{9}$$

where E and ν are the material Young's modulus and Poisson's ratio, respectively. The viscoelastic boundary (Deeks and Randolph 1994) is expressed as:

$$\boldsymbol{\sigma}_{\mathrm{n,s}} = -\rho \mathbf{C}_{n,s} \mathbf{v}_{n,s} - \mathbf{k}_{n,s} \mathbf{u}_{n,s} \tag{10}$$

where $\mathbf{u}_{n,s}$ is the vector of normal and shear displacements at the boundary and $\mathbf{k}_{n,s}$ is the spring stiffness matrix representing the elastic recovery of the infinite domain, which can be determined as follows:

$$\mathbf{k}_{n,s} = \frac{E}{2(1+\nu)} \begin{bmatrix} 2/r_b & 0 \\ 0 & 1/2r_b \end{bmatrix} \tag{11}$$

where r_b is the distance from the boundary to the excitation location.

3 Implementation

The standard viscous and viscoelastic conditions are implemented in MPM by converting the boundary stresses into tractions which are applied at boundary material points (i.e. material points at the outer layer). The equilibrium equation for the mentioned dynamic boundary conditions is:

$$\left(\mathbf{K} + \frac{\mathbf{4m}}{\Delta t^2} + \mathbf{K}_{vis} + \mathbf{K}_{rec}\right)\Delta\mathbf{u} = \mathbf{F}_{ext} - \mathbf{F}_{int} - \mathbf{F}_{kin} - \mathbf{F}_{vis} - \mathbf{F}_{rec} \tag{12}$$

where $\mathbf{K}_{vis}$ and $\mathbf{K}_{rec}$ are the viscous and recovery stiffness matrices computed as:

$$\mathbf{K}_{vis} = \frac{4}{\Delta t}\sum_{p=1}^{nmps} \rho_p l_p \mathbf{S}_{ip}^T(\mathbf{x}_p)\mathbf{T}^{\mathbf{T}}\mathbf{C}_{n,s}\mathbf{T}\mathbf{S}_{ip}(\mathbf{x}_p) \tag{13}$$

$$\mathbf{K}_{rec} = 2\sum_{p=1}^{nmps} l_p \mathbf{S}_{ip}^T(\mathbf{x}_p)\mathbf{T}^{\mathbf{T}}\mathbf{k}_{n,s}\mathbf{T}\mathbf{S}_{ip}(\mathbf{x}_p) \tag{14}$$

where l_p is half of a material point's support domain, $\mathbf{S}_{ip}$ is the GIMP shape function matrix and $\mathbf{T}$ is the transformation. Finally, $\mathbf{F}_{vis}$ and $\mathbf{F}_{rec}$ are the viscous and recovery forces at the boundary, respectively, and they are determined as follows:

$$\mathbf{F}_{vis} = -2\sum_{p=1}^{bmps} \rho_p l_p \mathbf{S}_{ip}^T(\mathbf{x}_p)\mathbf{T}^{\mathbf{T}}\mathbf{C}_{n,s}\mathbf{T}\mathbf{S}_{ip}(\mathbf{x}_p)\left(\frac{2\Delta\mathbf{u}}{\Delta t} - \mathbf{v}\right) \tag{15}$$

$$F_{\text{rec}} = -2\sum_{\text{p=1}}^{\text{nmps}} l_p \mathbf{S}_{ip}^T(\mathbf{x}_p)\mathbf{T}^{\mathbf{T}}\mathbf{k}_{n,s}\mathbf{T}\mathbf{S}_{ip}(\mathbf{x}_p)(\mathbf{u} + \Delta\mathbf{u}) \tag{16}$$

By neglecting the terms $\mathbf{K}_{rec}$ and $\mathbf{F}_{rec}$ in Eq. (12) the viscous formulation is obtained. The reader is directed to Phuong (2021) for a detailed derivation of the equations.

4 Numerical Examples

In this section, two benchmarks are used to assess the proposed boundary formulations. First, a 1D column under axial loading is used to study the boundary's performance. Then, a shallow foundation under repeated loading is presented to investigate the advantages of simulating the unbounded domain properly.

4.1 1D Column Benchmark

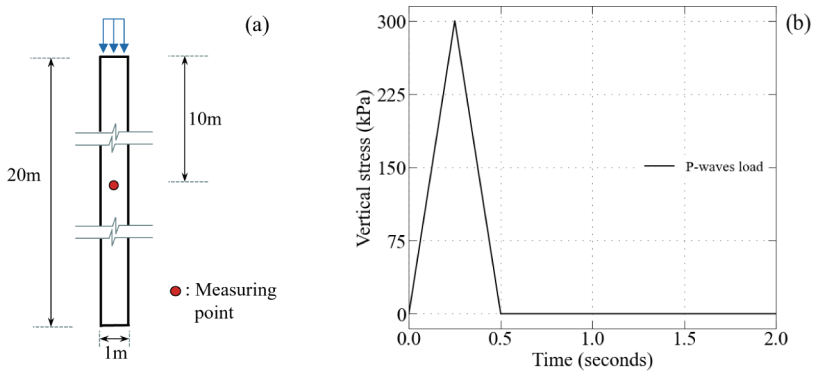

Fig. 1. (a) Schematic of the 1D benchmark with a measuring point, and (b) Delta load function

A 1D column of 20 m height and 1 m width under axial loading is investigated (Fig. 1a). A Delta load function with a maximum stress of 300 kPa and duration of 0.5 s is applied at the top of the column (Fig. 1b). The elastic parameters are Young's modulus $E = 20$ MPa, Poisson's ratio $\nu = 0.25$, and density $\rho = 1500$ kg/m^3. The background mesh is discretised using 2D square elements of size 0.25 m, in which each element contains initially 4 material points equally distributed. Figure 2b shows the stress recorded at the measuring point using different boundary conditions. The fixed boundary models (in dashed and solid black lines) show oscillations due to reflection with a peak stress of nearly 700 kPa (higher than the input load due to the combination of reflected and incoming waves). Using the dynamic boundaries, a peak stress of 300 kPa is obtained (equal to the Delta function) with almost all reflected waves being absorbed. While the viscous model perfectly absorbs the incoming waves, stress tension is observed after $t \approx 0.57$ s with the viscoelastic model due to the recovery of the boundary (Fig. 2b). The maximum displacement obtained with the fixed models is nearly 0.2 m, while the absorbing boundary models produce higher values of 0.4 m and 0.34 m with the viscous and viscoelastic conditions, respectively.

4.2 Foundation Under Repeated Loading

A 2D strip foundation of width $2B = 1.0$ m on a cohesive soil under repeated loading is studied. The soil domain has a depth of $H = 8B$ m and a width of $D = 12B$. The model is set up with 2 measuring points (point 1 and 2) as shown in Fig. 3a. The soil parameters are Young's modulus $E = 2000$ kPa, Poisson's ratio $\nu = 0.41$, and density $\rho = 1000$ kg/m^3. A time step of $\Delta t = 0.005$ s is used and the background mesh uses quadrilateral elements of size 0.0625 m.

The soil behaves as an elastic, perfectly plastic material, using a von Mises yield criterion incorporating post-peak softening in which the peak cohesion is $c_p = 10$ kPa

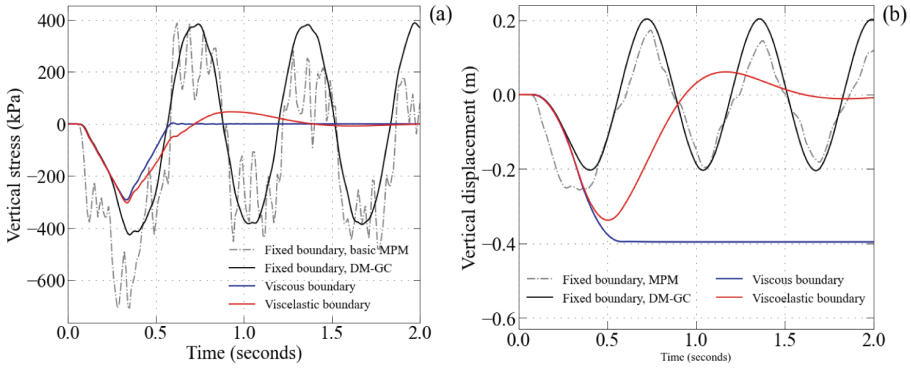

Fig. 2. Vertical stress at the measuring point (a) and Vertical displacement at the measuring point (b)

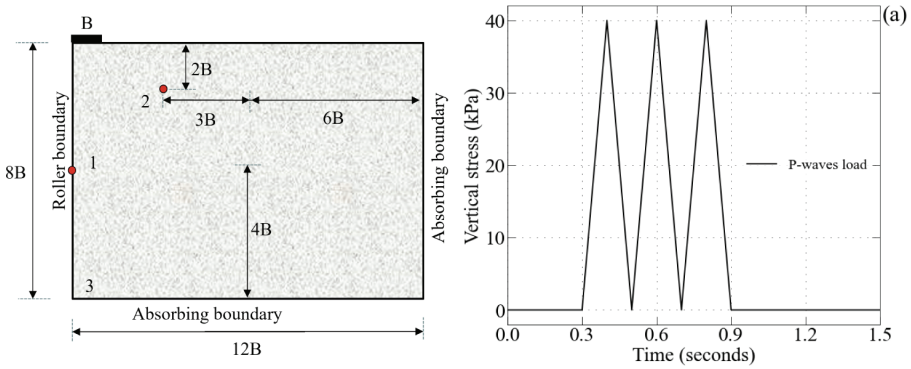

Fig. 3. Foundation model with measuring points 1 and 2 (a) and Repeated load (b)

and the residual strength is $c_r = 3$ kPa. Figure 3b shows the loading applied to the foundation. A quasi-static step is performed to generate initial stresses.

Figure 4 shows the plastic strains obtained using fixed and dynamic boundaries. It is observed that a primary shear band is fully developed for all 3 simulations, starting at the toe of the foundation, to a depth of $2B$ (with the fixed boundary model) and $4B$ (with the viscous and the viscoelastic boundary models). Additionally, the soil immediately beneath the foundation yields completely when using fixed boundaries due to the amplification effect, which creates larger stresses and results in more plastic strains, whereas with the remaining simulations no plastic strains are generated at this location. The fixed model also indicates that the secondary shear band is almost fully developed to the surface, while it is only partly generated with the dynamic boundary models. The soil below the foundation behaves more stiffly with the fixed model, which is why deeper plastic strain zones cannot fully develop as compared to the others models.

The vertical stress recorded at point 1 is given in Fig. 5a. It is observed that results for different boundaries are identical until time $t \approx 0.38$ s, after which oscillations are observed when fixed boundaries are used. In contrast, oscillations are non-existent

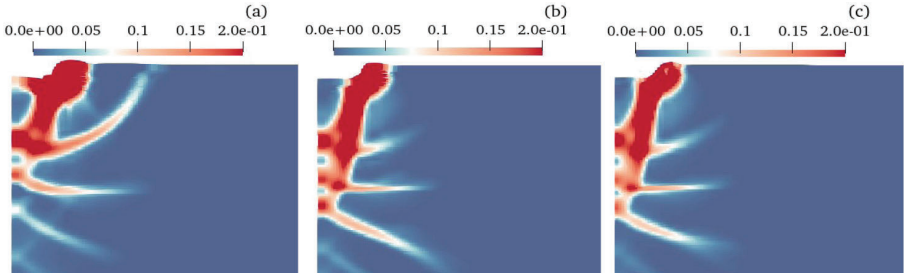

Fig. 4. Plastic strain at time $t = 0.925$ s below the foundation, using (a) fixed boundary with DM-GC, (b) viscous boundary with DM-GC, and (c) viscoelastic boundary with DM-GC

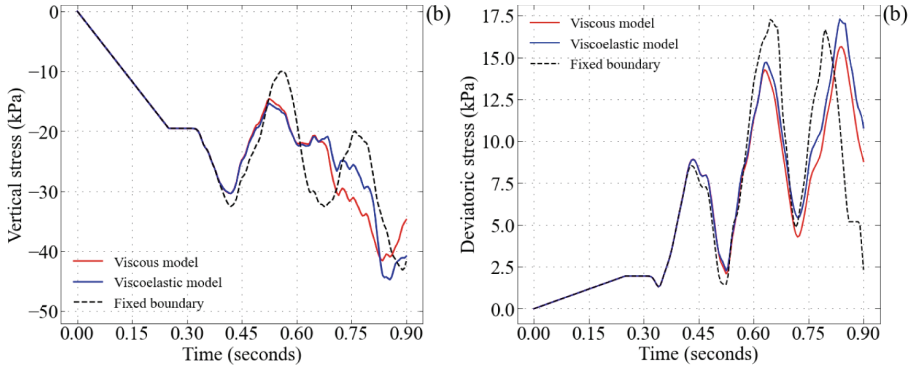

Fig. 5. (a) Vertical stress at point 1, and (b) Deviatoric stress at point 2 (b)

when the viscous (red line) and the viscoelastic (blue line) boundaries are used. This phenomenon causes the deviatoric stress of the fixed model to be higher (nearly 17.5 kPa at time $t \approx 0.63$ s) than those obtained with the dynamic models (14.9 kPa with the viscoelastic model and 14.5 kPa with the viscous model), as shown in Fig. 5b. Hence, more plastic strain is generated and the secondary shear band can fully develop.

5 Conclusions

This paper presents the implementation of two standard absorbing boundaries (viscous and viscoelastic) with an advanced MPM framework (i.e. DM-GC). The results of the 1D benchmark indicate that the spurious reflections induced by the fixed boundaries are eliminated almost completely using the dynamic boundaries. Furthermore, the viscoelastic boundary allows the recovery of the initial position of the bottom boundary. The geotechnical example shows that the absorbing boundaries lead to a higher quality solution, as the amplification effect is eliminated. The failure shear bands can be more accurately simulated since stress oscillations caused by the returning wave are removed.

References

Bardenhagen, S., Brackbill, J., Sulsky, D.: The material point method for granular materials. Comput. Methods Appl. Mech. Eng. **187**(3), 529–541 (2000)

Ceccato, F., Beuth, L., Vermeer, P.A., Simonini, P.: Two-phase material point method applied to the study of cone penetration. Comput. Geotech. **80**, 440–452 (2016)

Deeks, A.J., Randolph, M.F.: Axisymmetric time domain transmitting boundaries. J. Eng. Mech. **120**(1), 25–42 (1994)

Gonzalez Acosta, J.L., Vardon, P.J., Hicks, M.A.: Composite material point method (CMPM) to improve stress recovery for quasi-static problems. Proc. Eng. **175**, 324–331 (2017)

González Acosta, J.L., Vardon, P.J., Remmerswaal, G., Hicks, M.A.: An investigation of stress inaccuracies and proposed solution in the material point method. Comput. Mech. **65**(2), 555–581 (2020). https://doi.org/10.1007/s00466-019-01783-3

Lysmer, J., Kuhlemeyer, R.L.: Finite dynamic model for infinite media. J .Eng. Mech. Div. **95**(4), 859–877 (1969)

Phuong, C.D.: Implementing dynamic boundary conditions with the material point method. M.Sc. thesis, Delft University of Sciences and Technology, The Netherlands (2021)

Sulsky, D., Chen, Z., Schreyer, H.: A particle method for history-dependent materials. Comput. Methods Appl. Mech. Eng. **118**(1), 179–196 (1994)

Wang, B., Vardon, P.J., Hicks, M.A.: Investigation of retrogressive and progressive slope failure mechanisms using the material point method. Comput. Geotech. **78**, 88–98 (2016)

Zhou, S., Stormont, J., Chen, Z.: Simulation of geomembrane response to settlement in landfills by using the material point method. Int. J. Numer. Anal. Meth. Geomech. **23**(15), 1977–1994 (1999)